ACS APPLIED MATERIALS & INTERFACES

www.acsami.org

Forum Article

Understanding the Mechanical Reinforcement of Metal–Organic Framework–Polymer Composites: The Effect of Aspect Ratio

Xiaozhou Yang, Brittany L. Bonnett, Glenn A. Spiering, Hannah D. Cornell, Bradley J. Gibbons, Robert B. Moore, E. Johan Foster, and Amanda J. Morris*

Cite This: https://doi.org/10.1021/acsami.1c05430

Read Online

ACCESS | Metrics & More | Article Recommendations | Supporting Information

ABSTRACT: The aspect ratio (AR) of filler particles is one of the most critical determinants for the mechanical properties of particle-reinforced polymer composites. However, it has been challenging to solely study the effect of particle AR due to the difficulties of controlling AR without altering the physical and chemical properties of the particle. Herein, we synthesized PCN-222, a zirconium-based porphyrinic metal–organic framework (MOF) with preferential longitudinal growth as a series of particles with ARs increasing from 3.4 to 54. The synthetic MOF conditions allowed for the chemical properties of the particles to remain constant over the series. The particles were employed as reinforcers for poly(methyl methacrylate) (PMMA). MOF–polymer composite films were fabricated using doctor-blading techniques, which facilitated particle dispersion and alignment in the PMMA matrix, as revealed by optical microscopy and wide-angle X-ray diffraction. Mechanical measurements showed that both elastic and dynamic moduli increased with particle AR and particle concentrations but started to decrease as particle loading increased beyond 0.5 wt % (1.12 vol %). The data obtained at low particle loadings were fitted well with the Halpin–Tsai model. In contrast, the percolation model and the Cox model were unable to adequately fit the data, indicating the mechanical reinforcement in our system mainly originated from efficient load transfer between particles and the matrix in the particle orienting direction. Finally, we showed that the thermal stability of composite films increased with the addition of MOF particles because of the high thermal degradation temperature and restricted polymer chain mobility.

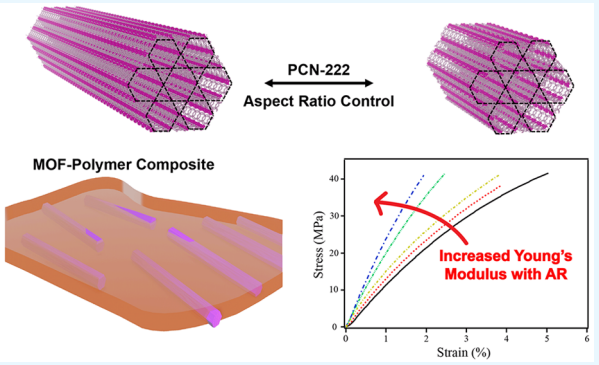

KEYWORDS: *metal–organic frameworks, polymer, polymer composite, mechanical reinforcement, mechanical model, aspect ratio*

INTRODUCTION

Lightweighting of materials was first introduced to decrease the cost of manufacturing and construction due to the scarcity of traditional raw materials. The unexpected consequence was increased research in the development of new materials classes such as engineered plastics, ceramics, and composites with great benefits across many industries.[1−4] Of these, polymer composites (PCs), a class of materials consisting of a polymer matrix and dispersed particulate phase, exhibit favorable properties, such as low mass and a wide range of mechanical performance.[5−9] Expansive research has been conducted to design PCs using a wide range of filler particles, including clays,[10−12] cellulose nanocrystals (CNCs),[13,14] carbon nanotubes (CNTs),[15−17] and graphene-related nanomaterials.[18,19] Mechanically reinforced PCs have been applied in a variety of industries, such as automotive manufacturing,[20−22] aerospace engineering,[23,24] and medical devices.[25,26]

The properties of PCs are governed by several aspects, including particle dispersion, particle orientation, particle–matrix interactions, particle shape, and particle aspect ratio (AR).[27] Among those, AR, defined as the ratio of the length to the diameter of rod-like particles or the length to the thickness of plate-like particles, is hypothesized to play the critical role in determining the mechanical performance of PCs. Increased particle AR is often associated with significant enhancement in the composite mechanical properties (e.g., composite Young's modulus, E_c), owing to efficient load transfer.[7,28−31] Effort has been devoted to correlate the mechanical properties of PCs and particle ARs using standard particles such as CNTs[32−41] and CNCs[42,43] because of their wide range of obtainable ARs. However, altering ARs of these materials often results in changed physical and/or chemical properties. With CNTs, one approach to produce different AR particles is to utilize physical methods such as ultrasonication, ball milling, and grinding.[44−46] Mechanical methods can separate and fragment

Special Issue: Emerging Materials for Catalysis and Energy Applications

Received: March 23, 2021
Accepted: May 21, 2021

CNTs into different lengths but also damage CNTs and change their morphology.[47] Another approach is to use chemical treatments, such as acid hydrolysis, to break CNTs into various ARs.[48] Chemical oxidation can lead to CNTs with a narrow size distribution; however, it changes their physical properties (e.g., defect level)[48] and introduces functionalities on the surface (e.g., carboxyl groups).[49−51] Furthermore, CNTs with high AR often become wavy in morphology, and such waviness is known to decrease the mechanical properties of the PC.[35,39,52,53] In the case of CNCs, obtaining different ARs often requires extraction of CNCs from different sources, which results in crystals with inherently different properties.[42,43] The alterations in the intrinsic properties of the CNTs and CNCs affect their mechanical properties and the interfacial interactions in composite systems; therefore, it has been very challenging to solely characterize the importance of AR on mechanical reinforcement of PCs.

Metal−organic frameworks (MOFs) are ideal candidates to study the effect of AR on mechanical reinforcement. MOFs are crystalline coordination polymers composed of metal clusters bridged by multidentate organic ligands, resulting in one-, two-, or three-dimensional porous networks.[54−56] The high porosity leads to the extremely low density exhibited by MOFs; for example, MIL-53-NH_2 and PCN-222 have densities of 0.35 and 0.52 g/cm^3, respectively,[57,58] substantially lower than most of the conventional fillers such as clay (2.9 g/cm^3)[59] and cellulose (1.5 g/cm^3).[60] The low density in turn leads to lightweight materials that, due to the other properties of MOFs, may possess multifunctionality and postsynthetic modification capability.[61,62] Therefore, MOFs have been incorporated into polymers to form composite materials for a variety of applications such as gas separation, water purification, and toxic chemical degradation.[63,64] In addition, MOFs can possess either isotropic or anisotropic growth behaviors depending on metal−linker composition and connectivity as well as synthetic parameters.[65,66] Tuning anisotropic growth of MOF particles has been a topic of recent interest in fields such as gas separation and catalysis.[67−69] We have recently demonstrated the tunability of AR and length for a zirconium-based porphyrinic MOF, PCN-222 ($Zr_6(\mu_3\text{-}O)_8(OH)_8(TCPP)_2$, where TCPP = *meso*-tetrakis(4-carboxyphenyl)porphyrin).[70] A wide range of AR was achieved (3.4 to 54) by facilitating anisotropic growth in the longitudinal direction (*c*-axis, Figure 1a), during which the surface chemistry and elemental composition of PCN-222 remain constant. Consistent chemistry, and therewith consistent surface chemistry in the resulting MOFs, is critical for retaining particle−matrix interactions and the mechanical properties of PCN-222. Therefore, we can isolate the impact of AR from other properties and investigate its effect on the mechanical behavior of composite films.

Herein, we fabricated MOF−polymer composite films consisting of poly(methyl methacrylate) (PMMA) as the matrix and PCN-222 with varying ARs as the reinforcer. The morphology of the films was characterized to reveal the dispersion and alignment of PCN-222 particles within a PMMA matrix. We then thoroughly investigated the elastic and dynamic moduli as well as thermal properties of the composite films, followed by fitting with mechanical models to unveil the reinforcing mechanisms and the relation with particle AR in the absence of other complicating factors.

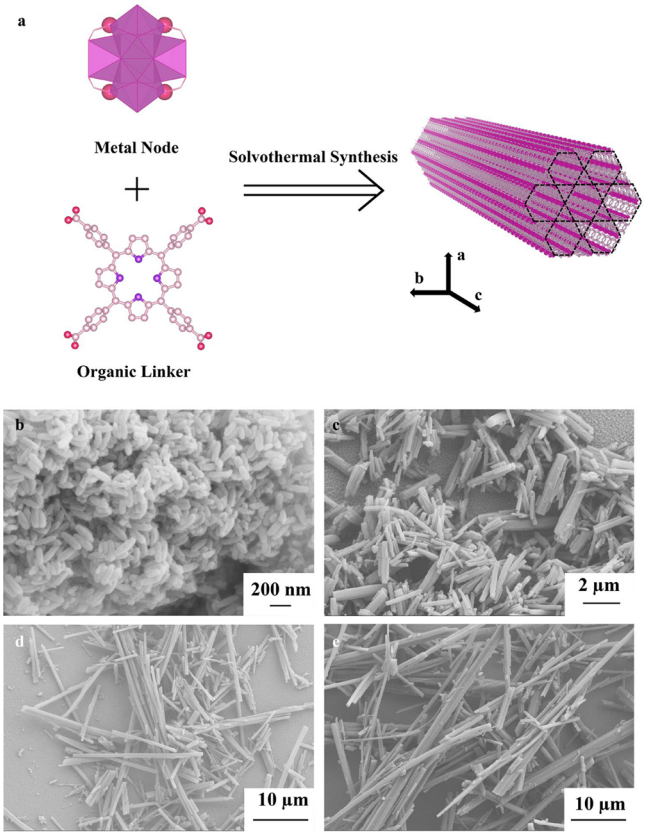

Figure 1. (a) Schematic illustration of PCN-222 formation and AR control. The organic linker, TCPP (purple = nitrogen, pink = carbon, red = oxygen), coordinates with the Zr metal node (red violet) through carboxylate groups to form rod-like PCN-222 particles growing along the *c*-axis (picture on the right, only carbon and Zr are displayed). (b−e) SEM images of PCN-222 particles with average AR of 3.4 (P-3.4, b), 7.8 (P-7.8, c), 31 (P-31, d), and 54 (P-54, e).

EXPERIMENTAL SECTION

Materials. All chemicals were purchased from commercial sources and used without further purification. Poly(methyl methacrylate) (PMMA, average M_w ∼ 120 000 g/mol) and zirconium(IV) oxychloride octahydrate ($ZrOCl_2{\cdot}8H_2O$, ≥99.5%) were purchased from Sigma-Aldrich (St. Louis, MO, United States). Chloroform (≥99.9%) and *N*,*N*-dimethylformamide (DMF, ≥99.9%) were obtained from Fischer Scientific (Hampton, NH, United States). Myristic acid (>99.9%) was purchased from Tokyo Chemical Industry Co., LTD (Tokyo, Japan). *meso*-Tetra(4-carboxyphenyl)porphyrin (TCPP, >97%) and difluoracetic acid (DFA, 98%) were purchased from Frontier Scientific (Logan, UT, United States) and Oakwood Chemical (Estill, SC, United States), respectively. Dimethyl sulfoxide-d_6 (DMSO-d_6) was obtained from Cambridge Isotope Laboratories (Andover, MA, United States).

PCN-222 Synthesis. PCN-222 was prepared via solvothermal synthesis using previously published procedures.[71] $ZrOCl_2{\cdot}8H_2O$, TCPP, and DFA were suspended in DMF in a 6-dram scintillation vial and then placed in a 120 °C oven for 18 h. The violet powder was isolated via centrifugation and washed 3× with DMF and acetone. Finally, the obtained MOF powders were dried in a vacuum oven at 60 °C overnight. Reagent amounts can be found in the Supporting Information (Table S1).

Postsynthetic Modification of PCN-222. PCN-222 was added to a 1 M myristic acid (MA) solution in DMF in a 10:1 stoichiometric ratio of MA to TCPP linker. The mixture was stirred at 60 °C for 18 h, isolated via centrifugation, washed 3× with DMF and acetone, and dried in a 60 °C oven overnight. MA loading was determined via ^{1}H

https://doi.org/10.1021/acsami.1c05430
ACS Appl. Mater. Interfaces XXXX, XXX, XXX−XXX

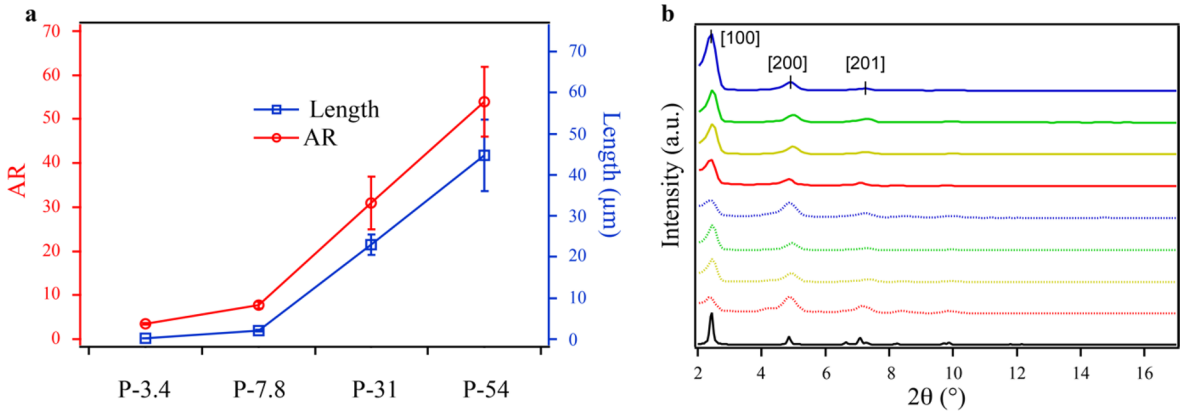

Figure 2. (a) AR and length analysis of PCN-222 obtained from SEM images using ImageJ software. (b) PXRD patterns of MA-functionalized PCN-222 (solid lines) with various ARs (blue: P-54, green: P-31, yellow: P-7.8, red: P-3.4) and respective as-synthesized PCN-222 (dashed lines). The simulated PXRD pattern of pristine PCN-222 is shown in black. Three distinctive crystal planes are highlighted.

NMR spectroscopy in DMSO-d_6 upon digestion of the MOF using concentrated H_2SO_4.

Powder X-ray Diffraction. Powder samples of PCN-222 were loaded on a Rigaku Si510 sample holder disc and inserted into a Rigaku Miniflex diffractometer (Cu Kα radiation λ = 1.5418 Å). PXRD measurements were collected over 2θ = 2−50° at a 0.05° resolution and a 1.0°/min continuous scanning mode.

^{1}H NMR Spectroscopy. PCN-222 (5 mg) was combined in a 2-dram scintillation vial with DMSO-d_6 (700 μL) and digested with two drops of concentrated H_2SO_4. The mixture was sonicated until fully dissolved and transferred to an NMR tube, where it was heated at 85 °C for 30 min in a sand bath and allowed to cool to room temperature. ^{1}H NMR spectra were collected on an Agilent U4-DD2 400 MHz NMR spectrometer.

Preparation of MOF-Polymer Composite Films. Various amounts of MA-modified PCN-222 particles were dispersed in 1.7 mL of chloroform in a 6-dram vial to obtain different weight loadings. The suspension was sonicated for 1 min to facilitate particle dispersion. A stir bar and 0.5 g of PMMA were added to the suspension, which was further sonicated for 1 min and stirred overnight. The order of chemicals added to the chloroform played an important role in determining the dispersion of PCN-222 particles. If PMMA was dissolved in chloroform prior to PCN-222 particles, the resultant highly viscous PMMA solution would not be able to disperse PCN-222 particles, despite post treatments such as ultrasonication and stirring. To fabricate the MOF−polymer composite films, the well-mixed dispersion was transferred to an acetone-cleaned glass slide and was manually cast via the doctor-blading technique. The as-cast suspension was then air-dried for 6 h and further annealed in a vacuum oven at 120 °C overnight. Finally, the resultant composite film was isolated by soaking the glass slide in water.

Scanning Electron Microscopy (SEM). For MOF particles, fluorine-doped tin oxide (FTO) slides were adhered to an SEM stage via double-sided copper tape. Carbon-conductive adhesive was applied to the sides of the FTO slides to increase the electrical conductivity. An acetone solution containing MOFs was drop-cast on the FTO slide and dried in air. All SEM stages were coated with a 7 nm thick Pt/Pd layer. Finally, SEM images were collected with a LEO 1550 field-emission scanning electron microscope (Carl Zeiss, Oberkochen, Germany) at 5.0 kV and a 7.0 mm working distance.

Dynamic Mechanical Analysis (DMA). Mechanical properties were obtained via the tension mode of DMA Q800 (TA Instruments, New Castle, DE, United States). The Young's moduli of the composite films were measured with the "DMA Controlled Force" mode at a 3 N/min force ramp rate at 25 °C. Two different testing methods under the "DMA multi-frequency-strain" mode were used to determine the dynamic moduli (storage and loss moduli) vs temperature relationship and the dynamic moduli at room temperature, respectively. The former was determined with the "Temp Ramp/Freq Sweep" method, where samples were held at 30 °C for 5 min before heating to 150 °C at 3 °C/min ramp rate and a frequency of 1 Hz. The later was performed under the "Isothermal Temp/Freq Sweep" method, where a 3 min soaking at 30 °C was employed for the films followed by 4 sweeps at 1 Hz. For all the mechanical measurements, the preload force was set to 0.02 N.

Thermogravimetric Analysis (TGA). TGA was used to determine the thermal stability of composite films and the decomposition of PCN-222. To remove residual solvent from PCN-222 particles, MOF powders were dried under vacuum at 120 °C overnight. A typical TGA measurement was performed with ∼10 mg samples (either films or PCN-222 particles) using a Q500 thermal analyzer (TA Instruments, New Castle, DE, United States) by heating from room temperature to 750 °C at 10 °C/min under nitrogen.

Optical Microscopy (OM). To gain information on the particle distribution within the PMMA matrix, a Nikon ECLIPSE LV100 (Nikon Instrument Inc., Tokyo, Japan) was used to obtain optical micrographs of the composite films. The images were taken under transmission mode.

Two-Dimensional Wide Angle X-ray Diffraction (2D WAXD). 2D WAXD experiments were performed using a Rigaku S-Max 3000 3 pinhole WAXD system equipped with a rotating anode emitting X-ray with a wavelength of 0.154 nm (Cu Kα). The sample-to-detector distance was 1005 mm for WAXD, and the q-range was calibrated using a silver behenate standard. The samples were placed in a sample stage perpendicular to the X-ray beam. Two-dimensional WAXD patterns were obtained using a 2D multiwire, proportional counting, gas-filled detector with an exposure time of 2 h. All of the WAXD data were analyzed using the SAXSGUI software package to obtain azimuthally integrated WAXD intensity versus azimuth for the scattering vector (q) range of 1.3- 2.2 nm^{-1} corresponding to the reflection characteristic of the (100) crystal planes of PCN-222, where $q = (4\pi/\lambda)\sin(\theta)$, θ is one-half of the scattering angle and λ is the X-ray wavelength. Hermans order parameter (S) was calculated according to previously reported literature:[72,73]

$$S = \frac{3\langle\cos^2\gamma\rangle - 1}{2} \quad (1)$$

$$\langle\cos^2\gamma\rangle = 1 - 2\langle\cos^2\phi\rangle \quad (2)$$

$$\langle\cos^2\phi\rangle = \frac{\int_0^{\pi} I(\phi)\sin\phi\cos^2\phi\,\mathrm{d}\phi}{\int_0^{\pi} I(\phi)\sin\phi\,\mathrm{d}\phi} \quad (3)$$

where the azimuthal angle, ϕ, is referenced from the drawing direction, and $I(\phi)$ is the scattering intensity as a function of ϕ.

https://doi.org/10.1021/acsami.1c05430
ACS Appl. Mater. Interfaces XXXX, XXX, XXX−XXX

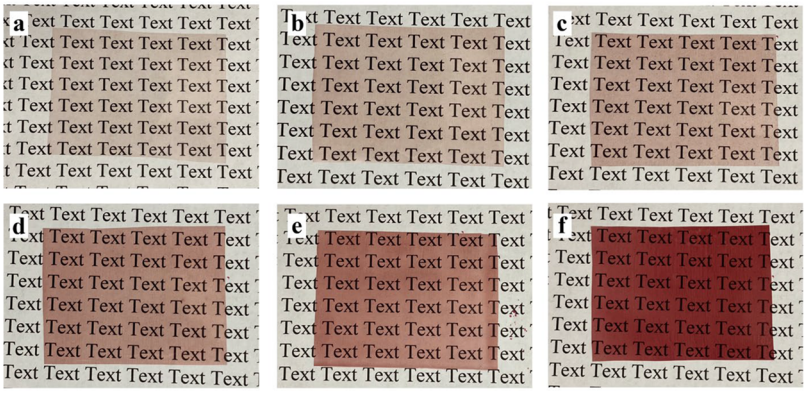

Figure 3. (a–f) Photographs of composite films (PMMA-54) filled with P-54 at different particle weight loadings: (a) 0.25 wt %, (b) 0.5 wt %, (c) 0.75 wt %, (d) 1 wt %, (e) 2 wt %, and (f) 4 wt %.

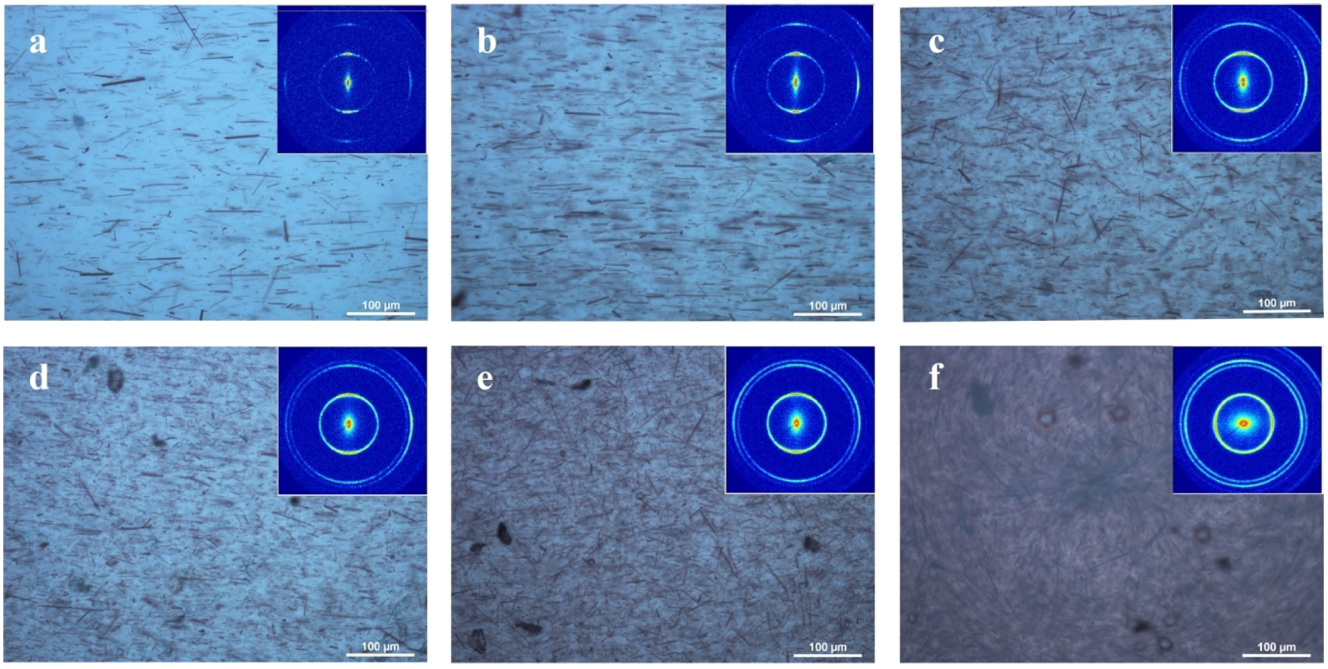

Figure 4. (a–f) Optical micrograph of (a) PMMA-54-0.25 wt %, (b) PMMA-54-0.5 wt %, (c) PMMA-54-0.75 wt %, (d) PMMA-54-1 wt %, (e) PMMA-54-2 wt %, and (f) PMMA-54-4 wt %. Scale bar: 100 μm. Insets: 2D WAXD data of the respective films.

RESULTS AND DISCUSSION

PCN-222 was selected as a filler for PMMA composites due to its highly tunable AR, low density (0.52 g/cm^3), and postsynthetic modification capabilities. Composed of Zr_6 oxo clusters bridged in an 8-connected fashion by TCPP ligands, PCN-222 exhibits preferential growth along the *c*-axis (Figure 1a). The resultant AR is controlled by modulated synthesis, in which a monocarboxylic acid (the modulator) competitively binds to the metal nodes and inhibits growth on the (100) and (010) facets. Selecting specific concentrations of the modulator and ligand results in PCN-222 rods with varying ARs, with growth on the (001) crystal face. MOF AR was confirmed by SEM analysis (Figure 1b–e and Figure 2a). The size dispersity of the particles increases as AR increases (e.g., P-31 and P-54), mainly due to the brittleness of the particle; these highly stiff and brittle MOF particles are more susceptible to breakage under processing steps (e.g., postsynthetic modification).

To increase the dispersity of MOF particles in organic solvent, as-synthesized PCN-222 underwent postsynthetic modification. The rods were functionalized with myristic acid (MA) via solvent-assisted ligand incorporation.[64] In this process, the carboxylate group on the MA binds to the metal node through substitution of a hydroxyl group. After MA incorporation, the ratio of MA to TCPP is determined to be 1.43 for a representative sample via ^{1}H NMR, indicating that MA is anchored not only at the MOF surface but also within the bulk (Figures S1 and S2). The alkyl chain from the MA provides organophilic character to the MOF surface, which is then available for interaction with organic solvent. The improved interaction increases the dispersity of MOF particles in organic solvent and thus facilitate film casting process and help produce higher quality composite films. Indeed, we observed that the composite Young's modulus (E_c) slightly increased after MA loading (Figure S3). The crystal structure was retained following functionalization of PCN-222 at all ARs as determined via PXRD (Figure 2b). ^{1}H NMR confirmed that the chemical structure of PCN-222 remained unchanged before and after MA loading (Figure S1).

https://doi.org/10.1021/acsami.1c05430
ACS Appl. Mater. Interfaces XXXX, XXX, XXX−XXX

Composite films were fabricated via doctor-blading. Briefly, MA-functionalized PCN-222 particles with different ARs were dispersed in chloroform to form a homogeneous dispersion. The dispersion was then used to fully dissolve PMMA powders. The well-mixed PCN-222/PMMA dispersion was transferred to an acetone-cleaned glass substrate, followed by a doctor-blade-assisted casting to form composite films. The films were annealed in a vacuum oven at 120 °C and labeled based on the particle AR and weight loading; for example, PMMA-54−0.25 wt % represents a PMMA composite film composed of PCN-222 with AR of 54 at 0.25 wt % loading. The resulting films exhibited uniform transparency, which is consistent with homogeneous dispersion and lack of macrophase separation (Figure 3).

A series of optical microscopic images of PMMA-54 at different particle loadings further confirmed that particles with high AR (e.g., P-54) were evenly distributed in the PMMA matrix without significant aggregation at most of the concentrations investigated (Figure 4a−e). At 4 wt % loading, however, particle agglomerates were observed, owing to the increased solution viscosity and particle−particle interactions as concentrations of PCN-222 increased (Figure 4f). More interestingly, the particles were found to be aligned in the doctor-blade drawing direction at low particle concentration (below 0.5 wt %, Figure 4a, b). As the concentration increased beyond 0.5 wt %, particle alignment decreased (Figure 4c−e). With the aid of 2D WAXD, we were able to quantitatively study particle alignment in the PMMA matrix. 2D WAXD probes crystalline information and provides diffraction patterns as Debye−Scherrer rings, whereas noncrystalline materials do not show diffraction patterns (e.g., pure PMMA film, Figure S4a). The anisotropy of the Debye−Scherrer rings shows the spatial orientation of the material, i.e., isotropic rings represent random orientation while arcs demonstrate an oriented sample.[74] For our composite films of PMMA-54 series, the diffraction patterns were confined into arcs oriented normal to the doctor-blade-drawing direction at low particle concentrations (Figure 4a, b insets) while they became more isotropic as the concentrations increased (Figure 4c−f insets). The increase in anisotropy of the Debye−Scherrer rings indicated better alignment of PCN-222 particles at low particle concentrations. The increased diffraction intensity correlated to increased particle concentration. As a comparison, pure PCN-222 powders showed homogeneous diffraction patterns with high intensity (Figure S4b). The orientation of particles was characterized by the Hermans order parameter (S) obtained from the intensity distribution in the azimuthal angle of diffraction.[72,73] In theory, S ranges from −0.5 to 1, with −0.5 resulting from crystals aligned perpendicular to the director, 0 meaning random orientation, and unity representing perfect alignment of crystals. To calculate S, we selected the diffraction signals of the (100) crystal plane of PCN-222 because it was parallel to the longitudinal axis and thus, could directly indicate the orientation of the MOF particles. All composite films showed several times higher values of S than PCN-222 powders and bare PMMA films (Figure 5). The highest S was obtained for PMMA-54-0.5 wt %, and it was comparable with previously reported values[73,75] yet lower than some other results.[72,74,76] Several factors can affect particle orientation, such as drawing speed, solution viscosity, and particle−polymer interactions.[74,77] We attribute PCN-222 alignment to the shearing force generated through doctor-blade drawing. The loss of alignment observed at higher concentrations was caused by increased particle−particle interactions which led to aggregation and a more isotropic distribution.[74,75]

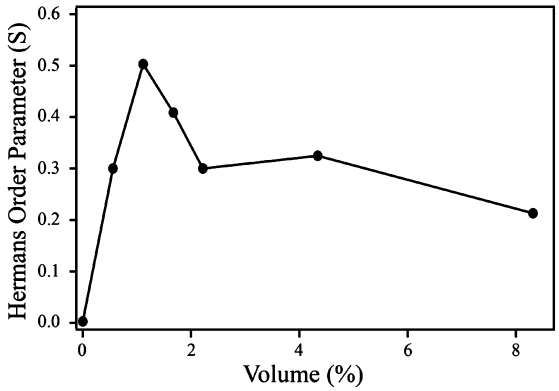

Figure 5. Hermans order parameter (S) of aligned PCN-222 rods within composite films obtained from WAXD. S of PCN-222 powders is 0.130.

Tensile testing was used to evaluate the mechanical properties of the MOF−polymer composite films and reveal the effect of particle AR on the mechanical behavior. The representative stress−strain curves of composite films filled with 0.5 wt % (1.12 vol %) PCN-222 with different ARs, are shown in Figure 6a. With the addition of PCN-222 particles, all composite films exhibited a higher initial slope of stress−strain curves compared to pristine PMMA. The increased slope of stress−strain curve indicated an enhanced composite Young's modulus (E_c), which was calculated from the slope of the initial linear region of stress−strain curve (typically within 1% strain). More importantly, particles with higher AR yield better reinforcement, as indicated by an increased slope in the order PMMA-3.4 < PMMA-7.8 < PMMA-31 < PMMA-54. The E_c at various particle concentrations (by volume %) showed that at low particle volume % (≤1.12 vol %), E_c increased with particle content and AR (Figure 6b). At higher concentrations (>1.12 vol %), however, E_c decreased and overlapped with each other for all the samples regardless of particle AR. The initial increase in E_c at low particle concentrations was attributed to the increased amount of PCN-222 particles in the matrix, while the following decline was due to the presence of particle aggregates (Figure 4f) and weak interactions at the particle−matrix interface, which could lead to formation of voids. Such defects could decrease interfacial friction and induce inefficient stress transfer, which resulted in weakened composite films.[37,38,78,79] We also noticed a decrease in both strength and elongation-at-break as the particle concentrations increased (Figure S6). The decrease of mechanical strength with increasing particle concentrations is well-known in the composite field and can also be explained by the formation of particle aggregates and the increased particle surface area providing defects to promote crack propagation.[78,80]

The effect of AR on E_c was estimated using the reinforcement factor (RF) calculated from E_c/E_m (E_m, matrix Young's modulus) at 1.12 vol % (0.5 wt %) (Figure S7a). The positive correlation between the RF and particle AR indicated that more efficient stress transfer was achieved with higher AR particles. Previous studies have mathematically predicted that the reinforcing efficiency would increase as AR increased from 10 to 70 and then continue to decrease as AR exceeded 70. The decrease in reinforcing efficiency with AR is caused by the

https://doi.org/10.1021/acsami.1c05430
ACS Appl. Mater. Interfaces XXXX, XXX, XXX−XXX

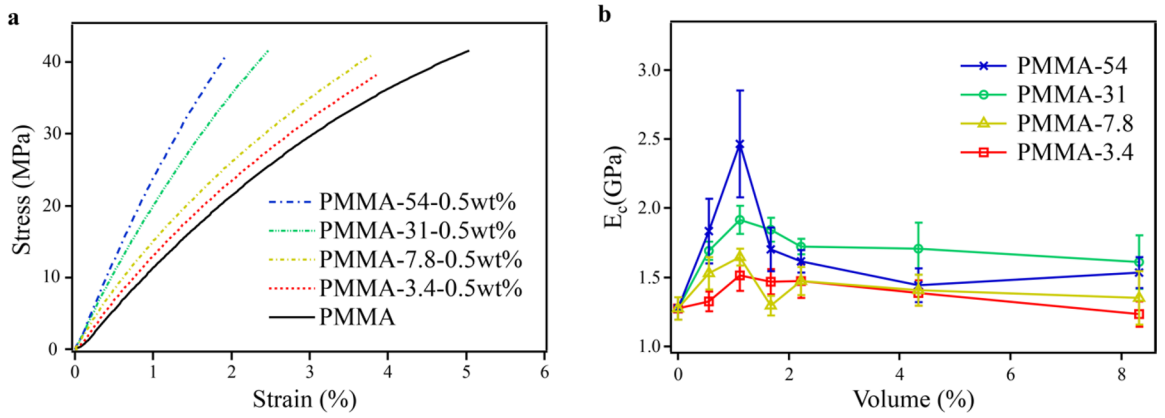

Figure 6. Tensile testing of MOF−polymer composite films. (a) Representative stress−strain curves of MOF−polymer composite films at 0.5 wt % MOF loading and control pure PMMA film. (b) Composite Young's modulus (E_c) with different filler ARs at various filler concentration (volume %). 0.25, 0.5, 0.75, 1, 2, and 4 wt % correspond to 0.56, 1.12, 1.67, 2.22, 4.34, and 8.32 volume %, respectively (details of concentration calculation can be found in the Supporting Information).

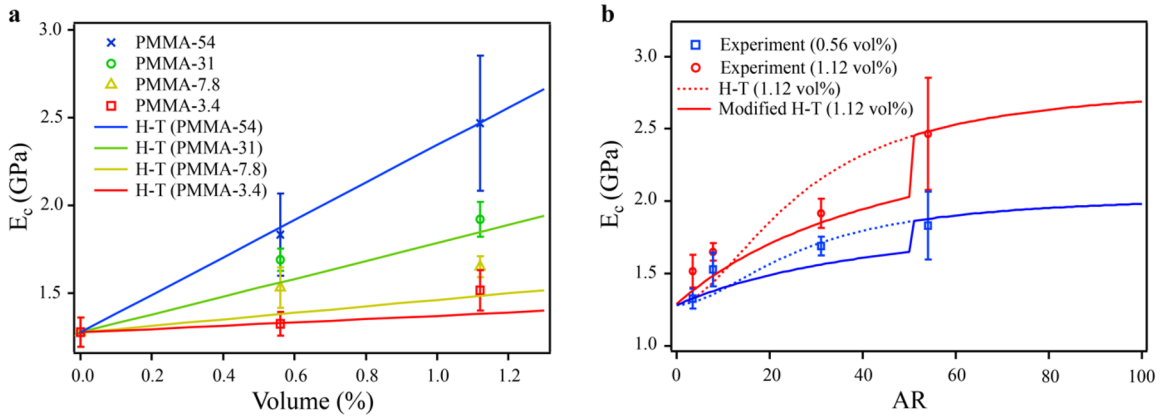

Figure 7. Data fitting with the Halpin-Tsai (H-T) model. (a) Composite Young's modulus (E_c) at low particle concentrations (markers) and the best H−T model fitting (solid line) by adjusting filler Young's modulus (E_f). (b) Composite Young's modulus (E_c) for 0.56 and 1.12 vol % filler concentration vs filler ARs. The dashed line represents the H−T model with shape factor $\xi = (0.5AR)^{1.8}$ at all ARs. The solid line shows modified H−T model with shape factor $\xi = (0.5AR)^{1.8}$ for ARs larger than 50 and $\xi = 2AR$ for ARs smaller than 50.

increased connectivity for high AR particles, which leads to a decrease in the effective AR for each individual particle and thus less efficient load transfer.[37,38,81] The PCN-222 particles used in this work possessed ARs ranging from 3.4 to 54, lower than the predicted threshold value of 70. Maximum E_c and RF were obtained for the sample PMMA-54-0.5 wt %, showing a E_c of 2.46 ± 0.39 GPa and a RF of nearly 2.0. The results were compared with other PMMA reinforcers reported in literatures (Figure 7b). Compared to other common reinforcers such as CNTs, CNCs, and graphene, our materials showed promising reinforcing performance at very low particle loading without polymer grafting (Figure S7b). Notably, Figure S7b shows that polymer-grafted fillers generally exhibit better reinforcement compared to nonmodified fillers. Such observation emphasizes the importance of the particle−matrix interactions because the polymer-grafted particles would possess enhanced interactions with polymer matrix.[27,80,82] The PCN-222 used in this study was only functionalized with MA, which did not provide significant interactions with the PMMA matrix but assisted particle dispersion in the casting solvent. Therefore, we hypothesize that PCN-222 reinforced polymer composites can be further enhanced by functionalizing the particle surface with polymers or functional groups that can provide strong specific interactions with the matrix (e.g., hydrogen bonding).

Mechanical models were applied to help understand the reinforcing mechanism of MOF-composite films. Attempting to do so, the filler Young's modulus (E_f), an important parameter in most of mechanical models and not available for PCN-222, needed to be determined. Because E_c could be experimentally measured, appropriate mechanical models could be selected to back-calculate E_f if the samples showed good agreement with the model assumptions.[14] The Halpin−Tsai (H−T) model describes a composite system consisting of oriented short fiber-like particles homogeneously dispersed in the polymer matrix.[15,16,83] Based on the observations obtained from optical microscopic images and WAXD data (Figure 3−5), our composite films exhibited similar morphology where the PCN-222 particles were orientated along the drawing direction within the PMMA matrix at low particle concentration (≤0.5 wt %). Therefore, it was reasonable to use the H−T model to calculate E_f. The model is expressed as:

$$E_c = \left(\frac{1 + \xi\eta\varphi_f}{1 - \eta\varphi_f}\right)E_m \quad (4)$$

https://doi.org/10.1021/acsami.1c05430
ACS Appl. Mater. Interfaces XXXX, XXX, XXX−XXX

$$\eta = \frac{\left(\frac{E_f}{E_m} - 1\right)}{\left(\frac{E_f}{E_m} + \xi\right)} \quad (5)$$

where φ_f represent the volume fraction of filler. ξ is the shape factor, given as 2AR for low AR (AR < 50) and $(0.5AR)^{1.8}$ for high AR (AR ≥ 50).[84−86] The initial three particle concentrations (0, 0.25, and 0.5 wt %), where particle alignment and mechanical reinforcement were observed, were fit with the H−T model. To find the best-fitting for E_f, the ξ values were calculated and held constant (Table 1); E_f was then fit across all four data sets simultaneously with the lowest fitting error. The fitting results showed that an E_f = 138 ± 12 GPa produced the best fit, and the resultant fitting curves at each AR are shown in Figure 7a. The calculated E_f value of PCN-222 was comparable to the simulated Young's modulus of MIL-47 (96.6 GPa) reported elsewhere.[57] The fitting errors, represented by the lowest residual sum of squares, are shown in Table 1 for all expressions. For better visualization, we plotted E_c vs AR at 0.56 and 1.12 vol % along with the predicted E_c by the H−T model using E_f = 138 GPa (Figure 7b). The dashed line represented H−T model with ξ = $(0.5AR)^{1.8}$ across all ARs, while the solid line showed the modified H−T model using the two expressions for ξ noted above. Similar approaches have been reported elsewhere to fit the experimental data obtained from polymer composites incorporating CNTs.[32−35] The unmodified H−T model fitted the data obtained at 0.56 vol %, while the modified H−T model showed closer agreement with results at 1.12 vol %. Overall, the unmodified and modified H−T models coincided well with the experimental data at low particle loadings (0.56 and 1.12 vol %). The good agreement at low loading was consistent with our observations of particle alignment and dispersion (*vide supra*), indicating the mechanical reinforcement in our system was mainly resulted from efficient load transfer between particles and the matrix in the particle orienting direction as proposed by the H−T model. In contrast, the model was unable to adequately fit the data at high particle loading (above 1.12 vol %, Figure S8a), at which the particle orientation decreased and started to deviate from the model's assumptions, and the imperfect particle−matrix interface also became more significant.

Table 1. Shape Factor (ξ) and the Residual Sum of Squares from Data Fitting with the H−T Model

sample	ξ	residuals
PMMA-3.4	ξ = 2AR = 6.8	0.01826
PMMA-7.8	ξ = 2AR = 15.6	0.05028
PMMA-31	ξ = 2AR = 62	0.02140
PMMA-54	$\xi = (0.5AR)^{1.8}$ = 377.1	0.00228

More comprehensive comparisons with other micromechanical models were performed to further understand the reinforcing mechanisms (details of calculation and fitting results can be found in the Supporting Information). We first

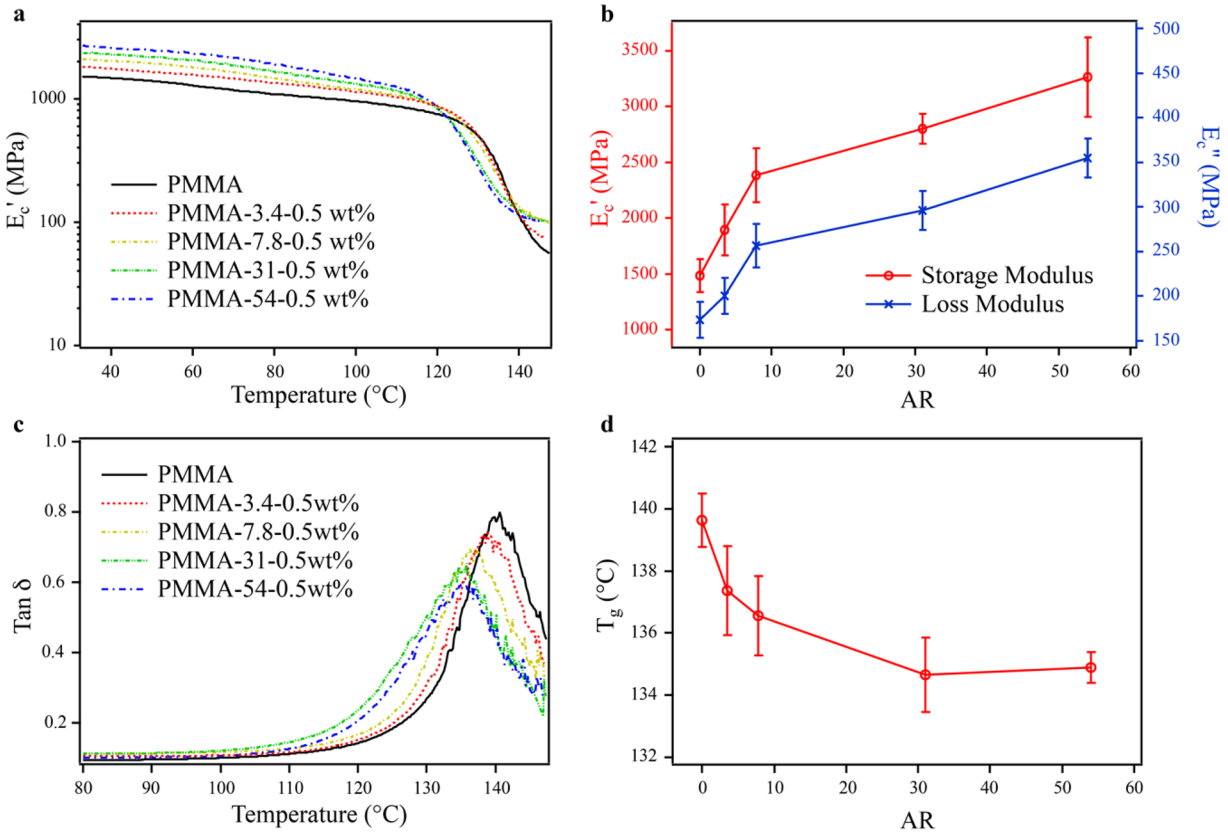

Figure 8. Dynamic test results of composite films. (a) Composite storage modulus (E_c') vs temperature at 0.5 wt % filler loading obtained from the "Temp Ramp/Freq Sweep" method. (b) Quantitative composite storage and loss modulus (E_c' and E_c'') vs filler's AR for films at 0.5 wt % particle loading with varying particle ARs. AR being zero represents PMMA films without particle addition. (c) tan δ vs temperature obtained from the data shown in panel a. (d) The peak positions of tan δ vs temperature plots are used to determine T_g.

https://doi.org/10.1021/acsami.1c05430
ACS Appl. Mater. Interfaces XXXX, XXX, XXX−XXX

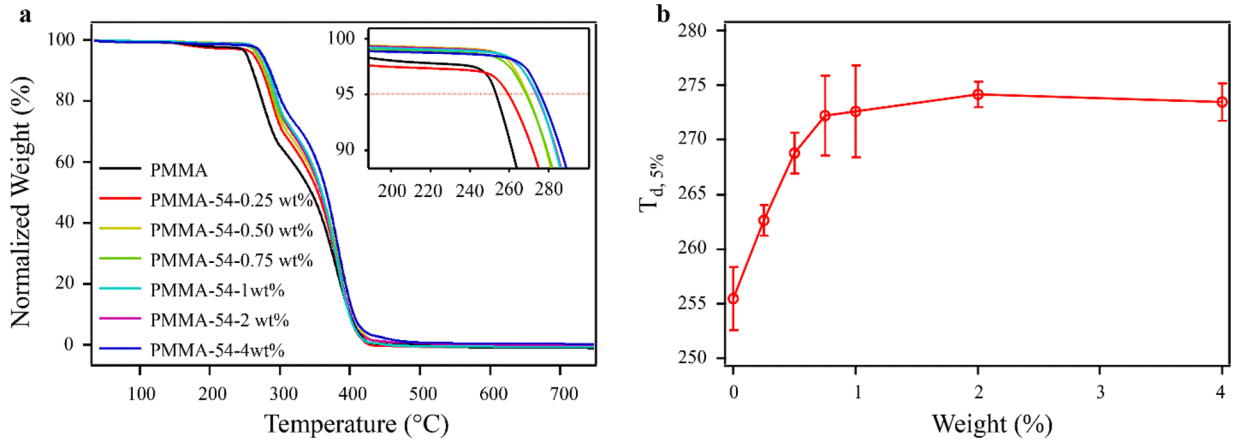

Figure 9. TGA results of composite films characterizing thermal stability. (a) TGA data of PMMA and PMMA-54 films at different weight loading. The experiments were conducted under N_2. Inset: Zoomed-in area from 200 to 300 °C. 95% normalized weight was highlighted. (b) Degradation temperature at 5% weight loss ($T_{d,5\%}$) for PMMA-54 as a function of particle weight percent.

used the modified Halpin−Tsai model (also called the Halpin−Kardos model) which hypothesized randomly oriented composites as quasi-isotropic laminates, consisting of short fibers uniaxially aligned within four laminates.[43,83,86] To account for random distribution, four laminates were set to orient at 0, 45, 90, and −45°. We found that the model underestimates E_c obtained from experimental results (Figure S8b). Because this unoriented H−T model considers the transverse Young's modulus as the main contribution of E_c and the longitudinal Young's modulus as the minor portion, it overlooks the reinforcement from the longitudinally aligned MOF particles. We further compared our data with the percolation model.[85] The percolation model assumes a network formed by interconnected particles after the particle concentration reaches a critical volume fraction.[87,88] The percolation threshold is directly related to AR and is given as 0.7/AR. The composite properties, such as mechanical stiffness and electric conductivity, would be largely increased upon reaching the percolation threshold. Our fitting results showed that the model yielded an underestimation of the experimental data and the percolation threshold occurred later than the actual reinforcement volume fraction, suggesting the absence of percolation network in our composite systems at low particle concentrations (Figure S8c). The absence of the percolation network was consistent with the lack of observed interconnected particles in the optical microscopic images. Finally, we used the Cox model, also known as the shear lag model, to study our data.[30,89−91] It provided a closer prediction of E_c as compared to the random H−T model and the percolation model; however, it still slightly underestimated the experimental E_c (Figure S8d). Such underestimation is mainly because of the inaccuracy of the orientation and length factor (η_o and η_l) assumed by the model. In addition, the predicted E_f by the H−T model might be imprecise, which might also contribute to the inaccuracy.

Because we discovered that the optimal E_c for our materials occurred at 0.5 wt % particle loading, this concentration was selected to study the relationship of particle AR and dynamic mechanical properties of composite films, namely storage (E') and loss modulus (E''). Consistent with E_c, E_c' also increased with particle AR, and all of the composite films exhibited reinforced E_c' compared to a pristine PMMA film (Figure 8a). We also performed multiple measurements at 1 Hz frequency while the chamber was held at 30 °C to gain more quantitative results. The results are summarized in Figure 8b, where both E_c' and E_c'' show similar trends with particle AR. The results further confirmed the positive correlation between mechanical properties and particle AR.

Interestingly, the DMA results indicated a shift in the onset of the glass transition to lower temperature as particle AR increased (Figure 8a). The tan δ (equal to E_c''/E_c') plots for the composite films were used to quantify the glass transition temperature (T_g) (Figure 8c, d). Previous research has shown that addition of unmodified particles into polymer matrices resulted in lower T_g due to weak particle−matrix interactions enabling chain mobility at the particle−matrix interface.[92−94] It was demonstrated that particles with higher specific surface area generate lower T_g. Therefore, one might predict that particles with low AR would exhibit lower T_g than the particles with high AR. In contrast, our results showed the opposite trend and lowering PCN-222 AR led to higher T_g. It was revealed that, unlike films made from high AR particles (e.g., P-54), low AR particles (e.g., P-3.4) tend to aggregate within the matrix, forming large assemblies with diameters around 6 μm (Figure S5), whereas larger particles showed less aggregation at same concentration (Figure 4b). The main cause of aggregation is the poor interaction between the PCN-222 and PMMA matrix because the short alkyl chains on the particle surface would cause dewetting.[82,95] Particle aggregation at low AR leads to a lower overall available interface, which may cause higher T_g.

Finally, the thermal stability of MOF−polymer composite films was probed by TGA. Representative TGA traces of PMMA-54 obtained under N_2 atmosphere are shown in Figure 9a. The initial weight loss occurring from 30 to 200 °C was attributed to solvent that was trapped within the MOF particles and the PMMA matrix. Pristine PCN-222 particles also showed a similar trend of weight loss from 100 to 170 °C (Figure S9a). Such results indicate that annealing of MOF-polymer composite films above polymer's T_g cannot fully remove residual solvents inside the pores of MOFs. The onset temperature of film degradation increased with MOF particle concentration, suggesting improved thermal stability imparted by MOF particles. The 95% normalized weight was highlighted to obtain the degradation temperature at 5% weight loss ($T_{d,5\%}$), which was a direct measurement of material thermal

https://doi.org/10.1021/acsami.1c05430
ACS Appl. Mater. Interfaces XXXX, XXX, XXX−XXX

stability (Figure 9a inset). We observed that $T_{d,5\%}$ increased with particle weight percent and reached a plateau of ~272 °C after 0.75 wt % (Figure 9b). As a comparison, $T_{d,5\%}$ of pure PMMA and PCN-222 were found to be 252 and 282 °C, respectively (Figure S9b). The improvement of the delayed degradation temperature of the polymer upon PCN-222 incorporation resulted from the higher thermal stability of the MOF particles (Figure S9). In addition, particle inclusion restricts chain mobility and reduces chain connectivity; therefore, the degradation temperature increases as the particle loading becomes higher.[9,96]

CONCLUSION

In this work, we elucidated the fundamental relationship between filler AR and polymer composite mechanical behavior with MOF particles. MOF synthesis conditions allow for consistent surface chemistry while modifying aspect ratio. In contrast, work with other filler particles is often limited in interpretation due to the change in both the chemical and physical properties of the fillers as AR is tuned. MOF−polymer composites with PCN-222 particles of varying ARs (3.4, 7.8, 31, 54) were fabricated and examined in terms of particle orientation and mechanical and thermal properties. The E_c increased with particle AR at low particle concentrations, and the results showed good agreement with the Halpin−Tsai model. The E_c decreased as the particle concentration increased due to the loss of particle alignment and particle agglomeration, which were indicated by optical microscopic images and Hermans order parameter calculated from 2D WAXD data. The addition of PCN-222 also impacted E_c' and E_c'', both of which exhibited increases with particle AR at 0.5 wt % loading. The thermal stability of PMMA was enhanced by the introduction of MOF particles, expanding advantages of MOF-polymer composites. Knowing the effect of particle AR on the composite mechanical properties can lead to the rational design of polymer composites and advance synthesis of novel particles for mechanical reinforcement. The successful fabrication of MOF−polymer composites with the promising mechanical reinforcement (RF ~ 2) at low particle weight loading showed great potential of applying MOFs as mechanical reinforcers, especially for lightweight materials.

ASSOCIATED CONTENT

Supporting Information

The Supporting Information is available free of charge at https://pubs.acs.org/doi/10.1021/acsami.1c05430.

NMR analysis of PCN-222, quantification of MA loading, mechanical enhancement by incorporating MA, structural characterization of control samples, tensile tests of MOF−polymer composite films, micromechanical model fitting, TGA of control samples (PDF)

AUTHOR INFORMATION

Corresponding Author

Amanda J. Morris − *Department of Chemistry, Virginia Tech, Blacksburg, Virginia 24060, United States; Macromolecules Innovation Institute, Virginia Tech, Blacksburg, Virginia 24061, United States*; Email: ajmorris@vt.edu

Authors

Xiaozhou Yang − *Department of Chemistry, Virginia Tech, Blacksburg, Virginia 24060, United States*

Brittany L. Bonnett − *Department of Chemistry, Virginia Tech, Blacksburg, Virginia 24060, United States*

Glenn A. Spiering − *Macromolecules Innovation Institute, Virginia Tech, Blacksburg, Virginia 24061, United States*

Hannah D. Cornell − *Department of Chemistry, Virginia Tech, Blacksburg, Virginia 24060, United States*

Bradley J. Gibbons − *Department of Chemistry, Virginia Tech, Blacksburg, Virginia 24060, United States*

Robert B. Moore − *Department of Chemistry, Virginia Tech, Blacksburg, Virginia 24060, United States; Macromolecules Innovation Institute, Virginia Tech, Blacksburg, Virginia 24061, United States;* orcid.org/0000-0001-9057-7695

E. Johan Foster − *Department of Chemistry, Virginia Tech, Blacksburg, Virginia 24060, United States; Macromolecules Innovation Institute, Virginia Tech, Blacksburg, Virginia 24061, United States; Department of Chemical and Biological Engineering, University of British Columbia, British Columbia, Vancouver V6T 1Z3, Canada;* orcid.org/0000-0002-4103-8510

Complete contact information is available at: https://pubs.acs.org/10.1021/acsami.1c05430

Notes

The authors declare no competing financial interest.

ACKNOWLEDGMENTS

The synthesis of high aspect ratio PCN-222 was work supported by the National Science Foundation under Grant 1551964. The electron microscopy was performed at the Nanoscale Characterization and Fabrication Laboratory, which is supported by the Virginia Tech National Center for Earth and Environmental Nanotechnology Infrastructure (NanoEarth), a member of the National Nanotechnology Coordinated Infrastructure (NNCI), supported by the NSF (ECCS 1542100 and ECCS 2025151). WAXD measurement was supported by the National Science Foundation under Grant DMR-1809291. DMA, TGA, and OM were made possible by the use of Virginia Tech's Materials Characterization Facility, which is supported by the Institute for Critical Technology and Applied Science, the Macromolecules Innovation Institute, and the Office of the Vice President for Research and Innovation. The authors thank Zacary L. Croft, Dong Guo, and Zhen Xu for their helpful discussion and assistance on DMA.

REFERENCES

(1) Plotkin, S. E. Examining Fuel Economy and Carbon Standards for Light Vehicles. *Energy Policy* **2009**, *37* (10), 3843−3853.

(2) Immarigeon, J.; Holt, R.; Koul, A.; Zhao, L.; Wallace, W.; Beddoes, J. Lightweight Materials for Aircraft Applications. *Mater. Charact.* **1995**, *35* (1), 41−67.

(3) Liebner, F.; Potthast, A.; Rosenau, T.; Haimer, E.; Wendland, M. Cellulose Aerogels: Highly Porous, Ultra-lightweight Materials. *Holzforschung* **2008**, *62* (2), 129−135.

(4) Cole, G.; Sherman, A. Lightweight Materials for Automotive Applications. *Mater. Charact.* **1995**, *35* (1), 3−9.

(5) Lau, K.-t.; Gu, C.; Hui, D. A Critical Review on Nanotube and Nanotube/Nanoclay Related Polymer Composite Materials. *Composites, Part B* **2006**, *37* (6), 425−436.

(6) Ku, H.; Wang, H.; Pattarachaiyakoop, N.; Trada, M. A Review on the Tensile Properties of Natural Fiber Reinforced Polymer Composites. *Composites, Part B* **2011**, *42* (4), 856−873.

(7) Ahmed, S.; Jones, F. A Review of Particulate Reinforcement theories for Polymer Composites. *J. Mater. Sci.* **1990**, *25* (12), 4933−4942.
(8) Sengupta, R.; Bhattacharya, M.; Bandyopadhyay, S.; Bhowmick, A. K. A Review on the Mechanical and Electrical Properties of Graphite and Modified Graphite Reinforced Polymer Composites. *Prog. Polym. Sci.* **2011**, *36* (5), 638−670.
(9) Saheb, D. N.; Jog, J. P. Natural Fiber Polymer Composites: a Review. *Adv. Polym. Technol.* **1999**, *18* (4), 351−363.
(10) Gao, F. Clay/Polymer Composites: the Story. *Mater. Today* **2004**, *7* (11), 50−55.
(11) Bitinis, N.; Hernández, M.; Verdejo, R.; Kenny, J. M.; Lopez-Manchado, M. A. Recent Advances in Clay/Polymer Nanocomposites. *Adv. Mater.* **2011**, *23* (44), 5229−5236.
(12) Jlassi, K.; Chehimi, M. M.; Thomas, S. *Clay-Polymer Nanocomposites*; Elsevier, 2017.
(13) Kargarzadeh, H.; Mariano, M.; Huang, J.; Lin, N.; Ahmad, I.; Dufresne, A.; Thomas, S. Recent Developments on Nanocellulose Reinforced Polymer Nanocomposites: A Review. *Polymer* **2017**, *132*, 368−393.
(14) Foster, E. J.; Moon, R. J.; Agarwal, U. P.; Bortner, M. J.; Bras, J.; Camarero-Espinosa, S.; Chan, K. J.; Clift, M. J.; Cranston, E. D.; Eichhorn, S. J.; Fox, D. M.; Hamad, W. Y.; Heux, L.; Jean, B.; Korey, M.; Nieh, W.; Ong, K. J.; Reid, M. S.; Renneckar, S.; Roberts, R.; Shatkin, J. A.; Simonsen, J.; Stinson-Bagby, K.; Wanasekara, N.; Youngblood, J. P. Current Characterization Methods for Cellulose Nanomaterials. *Chem. Soc. Rev.* **2018**, *47* (8), 2609−2679.
(15) Coleman, J. N.; Khan, U.; Blau, W. J.; Gun'ko, Y. K. Small but Strong: a Review of the Mechanical Properties of Carbon Nanotube−polymer Composites. *Carbon* **2006**, *44* (9), 1624−1652.
(16) Spitalsky, Z.; Tasis, D.; Papagelis, K.; Galiotis, C. Carbon Nanotube−polymer Composites: Chemistry, Processing, Mechanical and Electrical properties. *Prog. Polym. Sci.* **2010**, *35* (3), 357−401.
(17) Moniruzzaman, M.; Winey, K. I. Polymer Nanocomposites Containing Carbon Nanotubes. *Macromolecules* **2006**, *39* (16), 5194−5205.
(18) Du, J.; Cheng, H. M. The Fabrication, Properties, and Uses of Graphene/Polymer Composites. *Macromol. Chem. Phys.* **2012**, *213* (10−11), 1060−1077.
(19) Villar-Rodil, S.; Paredes, J. I.; Martínez-Alonso, A.; Tascón, J. M. Preparation of Graphene Dispersions and Graphene-polymer Composites in Organic Media. *J. Mater. Chem.* **2009**, *19* (22), 3591−3593.
(20) Holbery, J.; Houston, D. Natural-fiber-reinforced Polymer Composites in Automotive Applications. *JOM* **2006**, *58* (11), 80−86.
(21) Jacob, G. C.; Fellers, J. F.; Simunovic, S.; Starbuck, J. M. Energy Absorption in Polymer Composites for Automotive Crashworthiness. *J. Compos. Mater.* **2002**, *36* (7), 813−850.
(22) Friedrich, K.; Almajid, A. A. Manufacturing Aspects of Advanced Polymer Composites for Automotive Applications. *Appl. Compos. Mater.* **2013**, *20* (2), 107−128.
(23) Irving, P. E.; Soutis, C. *Polymer Composites in the Aerospace Industry*; Woodhead Publishing, 2019.
(24) Cantor, B.; Assender, H.; Grant, P. *Aerospace Materials*; CRC Press, 2015.
(25) Ramakrishna, S.; Mayer, J.; Wintermantel, E.; Leong, K. W. Biomedical Applications of Polymer-composite Materials: a Review. *Compos. Sci. Technol.* **2001**, *61* (9), 1189−1224.
(26) Wei, G.; Ma, P. X. Structure and Properties of Nano-hydroxyapatite/Polymer Composite Scaffolds for Bone Tissue Engineering. *Biomaterials* **2004**, *25* (19), 4749−4757.
(27) Kumar, S. K.; Krishnamoorti, R. Nanocomposites: Structure, Phase Behavior, and Properties. *Annu. Rev. Chem. Biomol. Eng.* **2010**, *1*, 37−58.
(28) Liu, H.; Brinson, L. C. Reinforcing efficiency of nanoparticles: A Simple Comparison for Polymer Nanocomposites. *Compos. Sci. Technol.* **2008**, *68* (6), 1502−1512.
(29) Facca, A. G.; Kortschot, M. T.; Yan, N. Predicting the Elastic Modulus of Natural Fibre Reinforced Thermoplastics. *Composites, Part A* **2006**, *37* (10), 1660−1671.
(30) Tucker, C. L., III; Liang, E. Stiffness Predictions for Unidirectional Short-fiber Composites: Review and Evaluation. *Compos. Sci. Technol.* **1999**, *59* (5), 655−671.
(31) Liu, B.; Feng, X.; Zhang, S.-M. The Effective Young's Modulus of Composites Beyond the Voigt Estimation due to the Poisson Effect. *Compos. Sci. Technol.* **2009**, *69* (13), 2198−2204.
(32) Qian, D.; Dickey, E. C.; Andrews, R.; Rantell, T. Load Transfer and Deformation Mechanisms in Carbon Nanotube-polystyrene Composites. *Appl. Phys. Lett.* **2000**, *76* (20), 2868−2870.
(33) Thostenson, E. T.; Chou, T.-W. On the Elastic Properties of Carbon Nanotube-based Composites: Modelling and Characterization. *J. Phys. D: Appl. Phys.* **2003**, *36* (5), 573.
(34) Morcom, M.; Atkinson, K.; Simon, G. P. The Effect of Carbon Nanotube Properties on the Degree of Dispersion and Reinforcement of High Density Polyethylene. *Polymer* **2010**, *51* (15), 3540−3550.
(35) Feng, Q.-P.; Shen, X.-J.; Yang, J.-P.; Fu, S.-Y.; Mai, Y.-W.; Friedrich, K. Synthesis of Epoxy Composites with High Carbon Nanotube Loading and Effects of Tubular and Wavy Morphology on Composite Strength and Modulus. *Polymer* **2011**, *52* (26), 6037−6045.
(36) Ayatollahi, M.; Shadlou, S.; Shokrieh, M.; Chitsazzadeh, M. Effect of Multi-walled Carbon Nanotube Aspect Ratio on Mechanical and Electrical Properties of Epoxy-based Nanocomposites. *Polym. Test.* **2011**, *30* (5), 548−556.
(37) Martone, A.; Formicola, C.; Giordano, M.; Zarrelli, M. Reinforcement Efficiency of Multi-walled Carbon Nanotube/epoxy Nano Composites. *Compos. Sci. Technol.* **2010**, *70* (7), 1154−1160.
(38) Martone, A.; Faiella, G.; Antonucci, V.; Giordano, M.; Zarrelli, M. The Effect of the Aspect Ratio of Carbon Nanotubes on Their Effective Reinforcement Modulus in an Epoxy Matrix. *Compos. Sci. Technol.* **2011**, *71* (8), 1117−1123.
(39) Jiang, Z.; Zhang, H.; Han, J.; Liu, Z.; Liu, Y.; Tang, L. Percolation Model of Reinforcement Efficiency for Carbon Nanotubes Dispersed in Thermoplastics. *Composites, Part A* **2016**, *86*, 49−56.
(40) Monajjemi, M.; Baheri, H.; Mollaamin, F. A Percolation Model for Carbon Nanotube-polymer Composites Using the Mandelbrot-Given Curve. *J. Struct. Chem.* **2011**, *52* (1), 54−59.
(41) Loos, M. R.; Manas-Zloczower, I. Reinforcement Efficiency of Carbon Nanotubes−Myth and Reality. *Macromol. Theory Simul.* **2012**, *21* (2), 130−137.
(42) Mariano, M.; Chirat, C.; El Kissi, N.; Dufresne, A. Impact of Cellulose Nanocrystal Aspect Ratio on Crystallization and Reinforcement of Poly (butylene adipate-co-terephthalate). *J. Polym. Sci., Part B: Polym. Phys.* **2016**, *54* (22), 2284−2297.
(43) Xu, X.; Liu, F.; Jiang, L.; Zhu, J.; Haagenson, D.; Wiesenborn, D. P. Cellulose Nanocrystals vs. Cellulose Nanofibrils: a Comparative Study on Their Microstructures and Effects as Polymer Reinforcing Agents. *ACS Appl. Mater. Interfaces* **2013**, *5* (8), 2999−3009.
(44) Wang, Y.; Wu, J.; Wei, F. A Treatment Method to Give Separated Multi-walled Carbon Nanotubes with High Purity, High Crystallization and a Large Aspect Ratio. *Carbon* **2003**, *41* (15), 2939−2948.
(45) Kukovecz, Á.; Kanyó, T.; Kónya, Z.; Kiricsi, I. Long-time low-impact ball milling of multi-wall carbon nanotubes. *Carbon* **2005**, *43* (5), 994−1000.
(46) Kónya, Z.; Zhu, J.; Niesz, K.; Mehn, D.; Kiricsi, I. End Morphology of Ball Milled Carbon Nanotubes. *Carbon* **2004**, *42* (10), 2001−2008.
(47) Lu, K.L.; Lago, R.M.; Chen, Y.K.; Green, M.L.H.; Harris, P.J.F.; Tsang, S.C. Mechanical Damage of Carbon Nanotubes by Ultrasound. *Carbon* **1996**, *34* (6), 814−816.
(48) Kim, D.-Y.; Yun, Y. S.; Bak, H.; Cho, S. Y.; Jin, H.-J. Aspect Ratio Control of Acid Modified Multiwalled Carbon Nanotubes. *Curr. Appl. Phys.* **2010**, *10* (4), 1046−1052.

https://doi.org/10.1021/acsami.1c05430
ACS Appl. Mater. Interfaces XXXX, XXX, XXX−XXX

(49) Zhang, J.; Zou, H.; Qing, Q.; Yang, Y.; Li, Q.; Liu, Z.; Guo, X.; Du, Z. Effect of Chemical Oxidation on the Structure of Single-walled Carbon Nanotubes. *J. Phys. Chem. B* **2003**, *107* (16), 3712−3718.
(50) Forrest, G. A.; Alexander, A. J. A Model for the Dependence of Carbon Nanotube Length on Acid Oxidation Time. *J. Phys. Chem. C* **2007**, *111* (29), 10792−10798.
(51) Liu, J.; Rinzler, A. G.; Dai, H.; Hafner, J. H.; Bradley, R. K.; Boul, P. J.; Lu, A.; Iverson, T.; Shelimov, K.; Huffman, C. B. Fullerene Pipes. *Science* **1998**, *280* (5367), 1253−1256.
(52) Li, C.; Thostenson, E. T.; Chou, T.-W. Effect of Nanotube Waviness on the Electrical Conductivity of Carbon Nanotube-based Composites. *Compos. Sci. Technol.* **2008**, *68* (6), 1445−1452.
(53) Deng, F.; Zheng, Q.-S.; Wang, L.-F.; Nan, C.-W. Effects of Anisotropy, Aspect ratio, and Nonstraightness of Carbon Nanotubes on Thermal Conductivity of Carbon Nanotube Composites. *Appl. Phys. Lett.* **2007**, *90* (2), 021914.
(54) Yaghi, O. M.; O'Keeffe, M.; Ockwig, N. W.; Chae, H. K.; Eddaoudi, M.; Kim, J. Reticular Synthesis and the Design of New Materials. *Nature* **2003**, *423* (6941), 705−714.
(55) Kitagawa, S.; Kitaura, R.; Noro, S. i. Functional Porous Coordination Polymers. *Angew. Chem., Int. Ed.* **2004**, *43* (18), 2334−2375.
(56) MacGillivray, L. R. *Metal-Organic Frameworks: Design and Application*; John Wiley & Sons, 2010.
(57) Ortiz, A. U.; Boutin, A.; Fuchs, A. H.; Coudert, F.-X. Anisotropic Elastic Properties of Flexible Metal-organic Frameworks: How Soft are Soft Porous Crystals? *Phys. Rev. Lett.* **2012**, *109* (19), 195502.
(58) Morris, W.; Volosskiy, B.; Demir, S.; Gándara, F.; McGrier, P. L.; Furukawa, H.; Cascio, D.; Stoddart, J. F.; Yaghi, O. M. Synthesis, Structure, and Metalation of Two Tew Highly Porous Zirconium Metal−organic Frameworks. *Inorg. Chem.* **2012**, *51* (12), 6443−6445.
(59) Mondol, N. H.; Jahren, J.; Bjørlykke, K.; Brevik, I. Elastic Properties of Clay Minerals. *Leading Edge* **2008**, *27* (6), 758−770.
(60) Eichhorn, S. J.; Dufresne, A.; Aranguren, M.; Marcovich, N.; Capadona, J.; Rowan, S. J.; Weder, C.; Thielemans, W.; Roman, M.; Renneckar, S. Current International Research into Cellulose Nanofibres and Nanocomposites. *J. Mater. Sci.* **2010**, *45* (1), 1−33.
(61) Tranchemontagne, D. J.; Mendoza-Cortés, J. L.; O'Keeffe, M.; Yaghi, O. M. Secondary Building Units, Nets and Bonding in the Chemistry of Metal−organic Frameworks. *Chem. Soc. Rev.* **2009**, *38* (5), 1257−1283.
(62) Furukawa, H.; Cordova, K. E.; O'Keeffe, M.; Yaghi, O. M. The Chemistry and Applications of Metal-organic Frameworks. *Science* **2013**, *341* (6149), 1230444.
(63) Kalaj, M.; Bentz, K. C.; Ayala, S., Jr; Palomba, J. M.; Barcus, K. S.; Katayama, Y.; Cohen, S. M. MOF−polymer Hybrid Materials: From Simple Composites to Tailored Architectures. *Chem. Rev.* **2020**, *120*, 8267−8302.
(64) Kitao, T.; Zhang, Y.; Kitagawa, S.; Wang, B.; Uemura, T. Hybridization of MOFs and Polymers. *Chem. Soc. Rev.* **2017**, *46* (11), 3108−3133.
(65) Tsuruoka, T.; Furukawa, S.; Takashima, Y.; Yoshida, K.; Isoda, S.; Kitagawa, S. Nanoporous Nanorods Fabricated by Coordination Modulation and Oriented Attachment Growth. *Angew. Chem.* **2009**, *121* (26), 4833−4837.
(66) Choi, S.; Kim, T.; Ji, H.; Lee, H. J.; Oh, M. Isotropic and Anisotropic Growth of Metal−Organic Framework (MOF) on MOF: Logical Inference on MOF Structure Based on Growth Behavior and Morphological Feature. *J. Am. Chem. Soc.* **2016**, *138* (43), 14434−14440.
(67) Masoomi, M. Y.; Beheshti, S.; Morsali, A. Shape Control of Zn (II) Metal−organic Frameworks by Modulation Synthesis and Their Morphology-dependent Catalytic Performance. *Cryst. Growth Des.* **2015**, *15* (5), 2533−2538.
(68) Sikdar, N.; Bhogra, M.; Waghmare, U. V.; Maji, T. K. Oriented Attachment Growth of Anisotropic Meso/Nanoscale Mofs: Tunable Surface Area and CO_2 Separation. *J. Mater. Chem. A* **2017**, *5* (39), 20959−20968.
(69) Huelsenbeck, L.; Westendorff, K. S.; Gu, Y.; Marino, S.; Jung, S.; Epling, W. S.; Giri, G. Modulating and Orienting an Anisotropic Zn-Based Metal Organic Framework for Selective CH4/CO2 Gas Separation. *Crystals* **2019**, *9* (1), 20.
(70) Bonnett, B. L.; Ilic, S.; Flint, K.; Cai, M.; Yang, X.; Cornell, H. D.; Taylor, A.; Morris, A. J. Mechanistic Investigations into and Control of Anisotropic Metal-Organic Framework Growth. *Inorg. Chem.* **2021**, under revision.
(71) Bonnett, B. L.; Smith, E. D.; De La Garza, M.; Cai, M.; Haag, J. V., IV; Serrano, J. M.; Cornell, H. D.; Gibbons, B.; Martin, S. M.; Morris, A. J. PCN-222 Metal−Organic Framework Nanoparticles with Tunable Pore Size for Nanocomposite Reverse Osmosis Membranes. *ACS Appl. Mater. Interfaces* **2020**, *12* (13), 15765−15773.
(72) Yoshiharu, N.; Shigenori, K.; Masahisa, W.; Takeshi, O. Cellulose Microcrystal Film of High Uniaxial Orientation. *Macromolecules* **1997**, *30* (20), 6395−6397.
(73) Wang, B.; Torres-Rendon, J. G.; Yu, J.; Zhang, Y.; Walther, A. Aligned Bioinspired Cellulose Nanocrystal-based Nanocomposites with Synergetic Mechanical Properties and Improved Hygromechanical Performance. *ACS Appl. Mater. Interfaces* **2015**, *7* (8), 4595−4607.
(74) Ureña-Benavides, E. E.; Kitchens, C. L. Wide-angle X-ray Diffraction of Cellulose Nanocrystal−alginate Nanocomposite Fibers. *Macromolecules* **2011**, *44* (9), 3478−3484.
(75) Reising, A. B.; Moon, R. J.; Youngblood, J. P. Effect of Particle Alignment on Mechanical Properties of Neat Cellulose Nanocrystal Films. *J-FOR* **2012**, *2* (6), 32−41.
(76) Diaz, J. A.; Wu, X.; Martini, A.; Youngblood, J. P.; Moon, R. J. Thermal Expansion of Self-organized and Shear-oriented Cellulose Nanocrystal Films. *Biomacromolecules* **2013**, *14* (8), 2900−2908.
(77) Urena-Benavides, E. E.; Brown, P. J.; Kitchens, C. L. Effect of Jet Stretch and Particle Load on Cellulose Nanocrystal−alginate Nanocomposite Fibers. *Langmuir* **2010**, *26* (17), 14263−14270.
(78) Tjong, S. C. Structural and Mechanical Properties of Polymer Nanocomposites. *Mater. Sci. Eng., R* **2006**, *53* (3−4), 73−197.
(79) Crosby, A. J.; Lee, J. Y. Polymer Nanocomposites: the "Nano" Effect on Mechanical Properties. *Polym. Rev.* **2007**, *47* (2), 217−229.
(80) Gonçalves, G.; Marques, P. A.; Barros-Timmons, A.; Bdkin, I.; Singh, M. K.; Emami, N.; Grácio, J. Graphene Oxide Modified with PMMA via ATRP as a Aeinforcement filler. *J. Mater. Chem.* **2010**, *20* (44), 9927−9934.
(81) Carman, G.; Reifsnider, K. Micromechanics of Short-fiber Composites. *Compos. Sci. Technol.* **1992**, *43* (2), 137−146.
(82) Kumar, S. K.; Jouault, N.; Benicewicz, B.; Neely, T. Nanocomposites with Polymer Grafted Nanoparticles. *Macromolecules* **2013**, *46* (9), 3199−3214.
(83) Halpin, J.; Kardos, J. Moduli of Crystalline Polymers Employing Composite Theory. *J. Appl. Phys.* **1972**, *43* (5), 2235−2241.
(84) Dalmas, F.; Cavaillé, J.-Y.; Gauthier, C.; Chazeau, L.; Dendievel, R. Viscoelastic Behavior and Electrical Properties of Flexible Nanofiber Filled Polymer Nanocomposites. Influence of Processing Conditions. *Compos. Sci. Technol.* **2007**, *67* (5), 829−839.
(85) Capadona, J. R.; Shanmuganathan, K.; Tyler, D. J.; Rowan, S. J.; Weder, C. Stimuli-responsive Polymer Nanocomposites Inspired by the Sea Cucumber Dermis. *Science* **2008**, *319* (5868), 1370−1374.
(86) van Es, M.; Xiqiao, F.; Van Turnhout, J.; Van der Giessen, E. In *Specialty Polymer Additives: Principles and Applications*; Al-Malaika, S., Golovoy, A. W., Wilkie, C. A., Eds.; Wiley-Blackwell: New York, 2001; pp 391−414.
(87) Favier, V.; Chanzy, H.; Cavaillé, J. Polymer Nanocomposites Reinforced by Cellulose Whiskers. *Macromolecules* **1995**, *28* (18), 6365−6367.
(88) Favier, V.; Cavaille, J.; Canova, G.; Shrivastava, S. Mechanical Percolation in Cellulose Whisker Nanocomposites. *Polym. Eng. Sci.* **1997**, *37* (10), 1732−1739.
(89) Wang, Z.; Ciselli, P.; Peijs, T. The Extraordinary Reinforcing Efficiency of Single-walled Carbon Nanotubes in Oriented Poly (vinyl alcohol) Tapes. *Nanotechnology* **2007**, *18* (45), 455709.

https://doi.org/10.1021/acsami.1c05430
ACS Appl. Mater. Interfaces XXXX, XXX, XXX−XXX

(90) Chen, S.; Schueneman, G.; Pipes, R. B.; Youngblood, J.; Moon, R. J. Effects of Crystal Orientation on Cellulose Nanocrystals−cellulose Acetate Nanocomposite Fibers Prepared by Dry Spinning. *Biomacromolecules* **2014**, *15* (10), 3827−3835.
(91) Young, K.; Blighe, F. M.; Vilatela, J. J.; Windle, A. H.; Kinloch, I. A.; Deng, L.; Young, R. J.; Coleman, J. N. Strong Dependence of Mechanical Properties on Fiber Diameter for Polymer− nanotube Composite Fibers: Differentiating Defect from Orientation Effects. *ACS Nano* **2010**, *4* (11), 6989−6997.
(92) Bansal, A.; Yang, H.; Li, C.; Benicewicz, B. C.; Kumar, S. K.; Schadler, L. S. Controlling the Thermomechanical Properties of Polymer Nanocomposites by Tailoring the Polymer−particle Interface. *J. Polym. Sci., Part B: Polym. Phys.* **2006**, *44* (20), 2944−2950.
(93) Ash, B.; Schadler, L.; Siegel, R. Glass Transition Behavior of Alumina/Polymethylmethacrylate Nanocomposites. *Mater. Lett.* **2002**, *55* (1−2), 83−87.
(94) Ash, B. J.; Siegel, R. W.; Schadler, L. S. Glass-transition Temperature Behavior of Alumina/PMMA Nanocomposites. *J. Polym. Sci., Part B: Polym. Phys.* **2004**, *42* (23), 4371−4383.
(95) Akcora, P.; Liu, H.; Kumar, S. K.; Moll, J.; Li, Y.; Benicewicz, B. C.; Schadler, L. S.; Acehan, D.; Panagiotopoulos, A. Z.; Pryamitsyn, V. Anisotropic Self-assembly of Spherical Polymer-grafted Nanoparticles. *Nat. Mater.* **2009**, *8* (4), 354−359.
(96) Hanu, L. G.; Simon, G. P.; Cheng, Y.-B. Thermal Stability and Flammability of Silicone Polymer Composites. *Polym. Degrad. Stab.* **2006**, *91* (6), 1373−1379.

https://doi.org/10.1021/acsami.1c05430
ACS Appl. Mater. Interfaces XXXX, XXX, XXX−XXX